



## RESEARCH ARTICLE

10.1029/2019JA026484

**Kelvin-Helmholtz Waves Magnetic Curvature and Vorticity: Four-Spacecraft Cluster Observations**Rungployphan Kieokaew<sup>1</sup> and Claire Foullon<sup>1</sup> <sup>1</sup>CGAFD, Mathematics, CEMPS, University of Exeter, Exeter, UK**Key Points:**

- Magnetic curvature and vorticity properties of KH waves forming on the duskside magnetopause are derived from four-spacecraft Cluster analyses
- The properties are characterized with changes in solar wind conditions and for various scales of tetrahedron size relative to KH wavelength
- The curvature radius measurement is found to be dependent on the tetrahedron size, consistent with predicted nonlinear spatial variations

**Correspondence to:**R. Kieokaew,  
rk359@exeter.ac.uk**Citation:**Kieokaew, R., & Foullon, C. (2019). Kelvin-Helmholtz waves magnetic curvature and vorticity: Four-spacecraft Cluster observations. *Journal of Geophysical Research: Space Physics*, 124. <https://doi.org/10.1029/2019JA026484>

Received 11 JAN 2019

Accepted 17 APR 2019

Accepted article online 1 MAY 2019

**Abstract** [1] Magnetopause Kelvin-Helmholtz (KH) waves are rich in complex magnetic and flow structures which are key to understand the role of these waves in facilitating the solar wind plasma transport into the Earth's magnetosphere. Four spacecraft in tetrahedral configuration provide the tools necessary for characterizing in situ magnetic geometry and vortical flow. We apply the tools on KH waves observed by Cluster inside an electron boundary layer on the duskside magnetopause. Magnetic curvature and flow vorticity properties of the KH waves are obtained for various solar wind conditions. Smaller curvature radius and higher-positive vorticity are found for longer wavelength. Changes in KH wavelengths observed with relatively fixed tetrahedron size allow us to resolve magnetic curvature in multiscales. For the first time in a space plasma, we report the dependence of the curvature radius measurement on the ratio of the tetrahedron size to the wavelength, consistent with nonlinear spatial variations of magnetic structures that would be resolved by nested cross-scale spacecraft tetrahedrons. Negative vorticity is found to develop in the rolled-up vortex, adjacent to positive vorticity in the vortex core. The strength of negative vorticity is found to increase with the solar wind proton density and proton bulk flow speed. This study provides observational evidence of multiscale magnetic structures and is useful for understanding the development of rolled-up vortex signatures during various stages of solar wind-controlled KH wave evolution.

**1. Introduction**

Four-spacecraft analyses allow us to resolve in situ spatial and temporal dimensions of space plasmas. Cluster is the first four-spacecraft mission launched in 2000 to study the Earth's magnetospheric environments (Escoubet et al., 2001). Under northward interplanetary magnetic field (IMF) conditions, the Earth's magnetospheric boundaries along the flanks can be unstable to Kelvin-Helmholtz (KH) instability. KH instability can induce surface waves on the flank magnetopause, which may facilitate solar wind plasma transport across the magnetopause through secondary mechanisms such as magnetic reconnection (e.g., Nakamura & Fujimoto, 2008; Nykyri & Otto, 2001) and turbulence (e.g., Matsumoto & Hoshino, 2004; Rossi et al., 2015). Recently, a cross-scale energy transport from fluid to ion scales, a fundamental problem in plasma physics, has been reported within a KH vortex using Cluster observations (Moore et al., 2016; Retinò, 2016). KH waves can also be observed in other environments such as in the solar corona at the flank of a coronal mass ejection (Foullon et al., 2011) and in a prominence (Hillier & Polito, 2018). They are also observed in other planetary magnetospheric boundaries such as those of Mercury (e.g., Slavin et al., 2008) and Saturn (e.g., Masters et al., 2010). Studying KH waves at the Earth's magnetopause has the advantage that in situ multispacecraft measurements are much more accessible than in any other environment.

The KH instability bends magnetic fields and induces vortical flows in the magnetopause boundary layers. Magnetic and flow structures are ubiquitous in the Earth's magnetospheric environments and are best studied using multispacecraft observations. In particular, four-spacecraft techniques provide qualitative properties of space plasmas that are difficult to resolve by single-spacecraft methods. However, understanding applications and limitations of four-spacecraft techniques is essential to interpret their outputs. Kieokaew et al. (2018, K18 hereafter) applied magnetic curvature analysis (MCA; Shen et al., 2003) and vorticity analysis (Chanteur, 1998) techniques on magnetohydrodynamics simulations of magnetopause KH waves. In particular, they applied the techniques using various sizes of the four-spacecraft tetrahedron with a fixed KH wavelength. Multiscale structural analyses of the KH process are a first step to a physical cross-scale understanding. K18 show spatial characteristics of magnetic curvature and flow vorticity of the simulated KH waves in the magnetospheric context, near the equatorial plane where the conditions are KH-unstable,

©2019. The Authors.

This is an open access article under the terms of the Creative Commons Attribution License, which permits use, distribution and reproduction in any medium, provided the original work is properly cited.

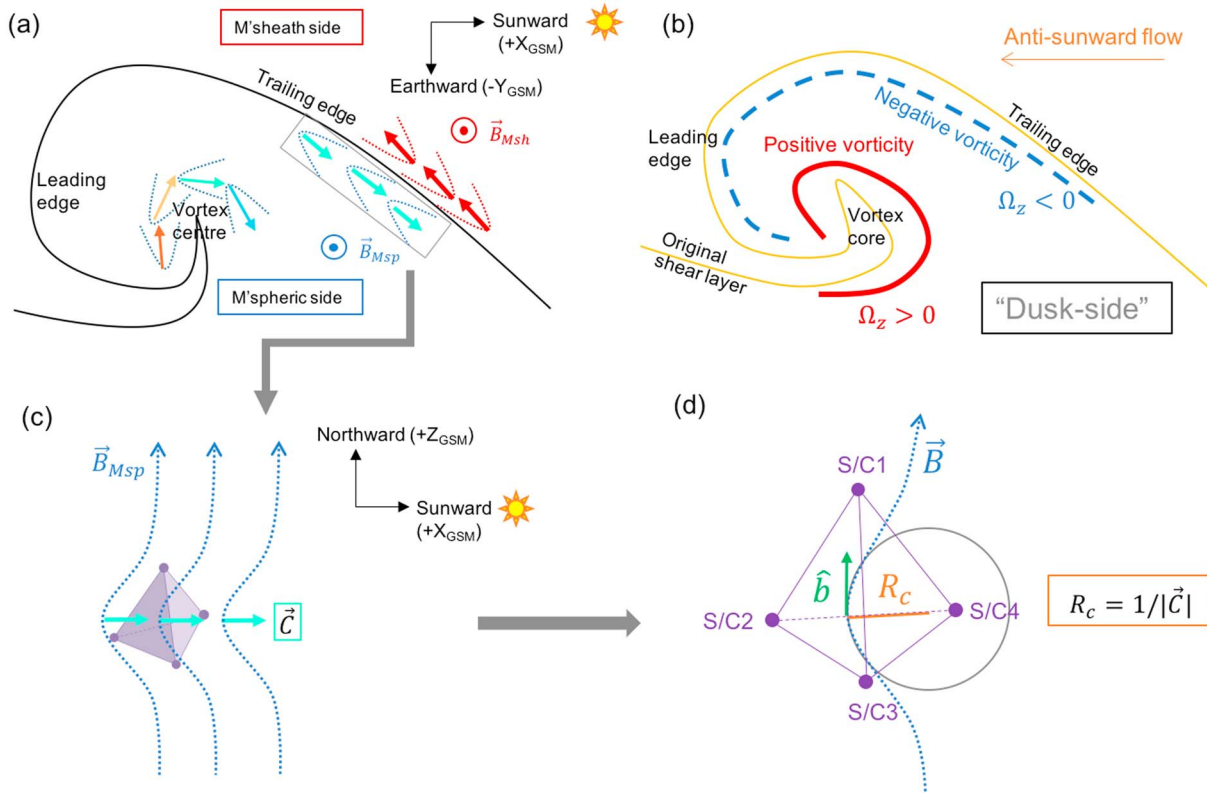


**Figure 1.** Sketch of (a) magnetic curvature directions and (b) flow vorticity of a rolled-up Kelvin-Helmholtz vortex developed on the duskside magnetopause; and (c and d) illustrations of the magnetic curvature analysis technique. (a) Curvature directions (colored vectors) point in opposite directions across the wave trailing edge and turn in a clockwise sense around the vortex center. (b) Vorticity is positive and strong around the vortex core, while it is negative and weak between the vortex core and the original shear layer. (c) Magnetic curvature ( $\vec{C}$ ) of the local magnetic field is resolved at the center of tetrahedron. (d) The corresponding curvature radius ( $R_c$ ) is retrieved from  $1/|\vec{C}|$  which is equal to the radius of a circle that can be fitted into the curved magnetic field line.

as illustrated in Figure 1. For example, small radii of curvature are found along the KH wave trailing edges (sunward facing) in the magnetospheric boundary layer as shown in Figure 1a (see also Figures 1c and 1d). For a rolled-up vortex developed on the duskside magnetopause, negative flow vorticity is expected to form between the strong positive flow vorticity of the vortex core and the positive flow vorticity of the original shear layer as shown in Figure 1b. This negative vorticity feature persists through the nonlinear development stage. Such expected signatures have yet to be confirmed in real observations.

Four-spacecraft measurements are sensitive to the distances between spacecraft. This was demonstrated in K18, who found that the measures of four-spacecraft signatures of the magnetopause KH waves are depending on the tetrahedron size. This is because plasma structures have nonlinear variations in the spatial dimension (e.g., see Figure 1c). They proposed two scenarios as examples of the nonlinear spatial variations of a magnetic structure that lead to (1) increasing and (2) decreasing radius of curvature measurements (see their Figure 4). Of particular interest is the numerical result that the measure of radius of curvature (Figures 1c and 1d) should increase linearly with the tetrahedron size when the ratio of the tetrahedron size,  $a$ , to the KH wavelength,  $\lambda_{KH}$ , is between 0.075 and 0.25. Such ratios are easily achieved with Cluster at the magnetopause. The magnetic curvature in the simulation erratically varies with the tetrahedron size outside this range, possibly due to complex structures in small ( $a/\lambda_{KH} < 0.075$ ) and large ( $a/\lambda_{KH} > 0.25$ ) scales. Nevertheless, some qualitative features of the magnetopause KH waves are shown to be less sensitive to the tetrahedron size such as magnetic curvature direction and flow vorticity polarity (as those sketched in Figures 1a and 1b). With these simulated preliminaries in mind, we are now looking for observational confirmation of nonlinear spatial variations of plasma structures associated with the Earth's flank magnetopause KH waves.

We choose KH observations on the dusk flank magnetopause by Cluster from the 20–21 November 2001 event. The coexistence of cold solar wind and hot magnetospheric ion populations in the vortices is first

reported as evidence of solar wind plasma transport during the nonlinear stage of the waves by Hasegawa et al. (2004). Magnetic and velocity perturbations are reported to be consistent with rolled-up vortices for a 16-min interval that is later confirmed by Hasegawa et al. (2006) using a single-spacecraft method (Takagi et al., 2006). Chaston et al. (2007) report evidence of diffusive transport across the magnetopause due to mode conversion from surface to kinetic Alfvén waves that is sufficient to account for the boundary layer formation. Foullon et al. (2008, F08 hereafter) characterize the evolution of the KH waves with the boundary layer thickness, geomagnetic latitude, and IMF clock angle (defined by the clockwise angle between the IMF orientation and the geomagnetic north direction) by utilizing the exceptionally prolonged KH activity of about 17 hr. They select five 2-hr intervals of relatively steady solar wind conditions but with different IMF clock angles. In particular, using four-spacecraft methods, they report the dependence of KH wavelengths and maximum spectral power on the IMF clock angle, consistent with Farrugia et al. (1998). We also note a work by Shen et al. (2012) in which they employ multiple-point analysis tools and use the same short interval as Hasegawa et al. (2004) for illustrations of flow vorticity and current density calculated from a three-spacecraft method.

The Cluster 20–21 November 2001 event, as previously analyzed by F08, allows us to benchmark the four-spacecraft methods for identifying rolled-up KH vortices, as proposed by K18. The resolved characteristics relate to physical phenomena that previous studies did not explore. Moreover, the different KH wavelengths and amplitudes (controlled by IMF clock angle) in the five intervals in F08 allow us to characterize KH properties at various scales. Indeed, the different KH wavelengths are observed with a four-spacecraft tetrahedral configuration that can be considered of fixed size during the event and relative to the wavelength changes. This is opposite to the approach in the numerical study of K18, where the size of the virtual tetrahedron is varied relative to a given wavelength from a single KH event. These two approaches are equivalent in that they allow us to study variations in KH wave properties for changes in the  $a/\lambda_{\text{KH}}$  ratio. Therefore, the new observational approach allows us to probe the KH waves in five “nested” scales with the aim to provide evidence for the nonlinear spatial variations of KH structures.

In this paper, we will resolve three-dimensional spatial characteristics of magnetopause surface waves with four identical spacecraft forming a tetrahedral configuration that detail multiscales of plasmas. We first investigate the magnetic curvature of simple boundary layer crossings of KH waves. The short interval in Hasegawa et al. (2004) and Shen et al. (2012) is revisited to benchmark applications of the four-spacecraft tools. We then compare four-spacecraft analysis results for different scales of KH waves subjected to various IMF clock angle conditions, as characterized in F08.

## 2. Data and Methodology

We investigate KH wave properties during the northward IMF conditions on 20–21 November 2001. Cluster entered the electron boundary layer (EBL) from the magnetosheath side at 09:15 UT on 20 November 2001 and exited the EBL to the magnetosphere at 03:00 UT on 21 November 2001. For this time interval, Cluster was in the EBL and did not cross the magnetopause. F08 characterize the KH activity into five intervals: A (10:00–12:00 UT), B (15:00–17:00 UT), C (18:04–20:04 UT), D (19:45–21:45 UT), and E (23:36–01:36 UT) with different IMF clock angle, solar wind proton bulk flow speed, and proton density. The solar wind conditions for each 2-hr interval are those tabled in F08, given in the observation frame of Cluster (see our Table 2). They were derived from the NASA High-Resolution OMNI product that is initially measured by the Advanced Composition Explorer satellite and time shifted to a model bow shock nose. Since not all on board instruments of Cluster (C1, C2, C3, and C4) were operative, we obtain plasma conditions as follows. Magnetic field data are provided by the Flux Gate Magnetometer instruments on C1–C4. Ion density, temperature, and bulk velocity data are provided by the Composition and Distribution Function analyzer instruments on C1, C3, and C4. Kinetic pressure is provided by the Hot Ion Analyzer instrument on C1 and C3. Original data are obtained in geocentric solar magnetospheric (GSM) system and transformed to the local boundary coordinates (LMN) using transformations given in F08 and derived from a model magnetopause (Roelof & Sibeck, 1993). In this LMN coordinates, **N** is perpendicular to the unperturbed model magnetopause pointing away from the Earth, **L** points along  $\mathbf{Z}_{\text{GSM}}$ , and **M** completes the system (which is in the sunward direction for the dusk event).

The following information is important to understand and to justify four-spacecraft results. We use the KH wavelengths derived by F08 from applying the timing analysis onto the wave leading and trailing edges (see

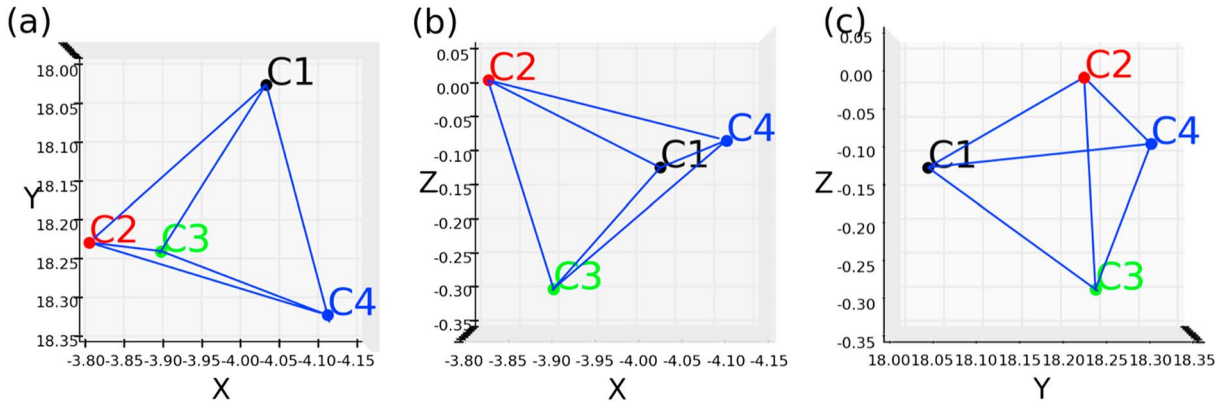


**Figure 2.** Two-dimensional projections in (a)  $X$ - $Y$ , (b)  $X$ - $Z$ , and (c)  $Y$ - $Z$  planes of the average Cluster positions in Earth radii on 20–21 November 2001 during 9 and 3 UT in GSM coordinates. GSM = geocentric solar magnetospheric system.

Figure 1a), in which the boundary normal speeds are obtained and projected onto the wave propagation direction. These KH wavelengths are proportional to the spectral power of the waves that correspond to the wave amplitudes (Foullon et al., 2010). The average interspacecraft separation during the event under study is  $2,000 \pm 93$  km. Considering dominant KH wavelengths which are 1.5–2.9 Earth radii ( $R_E$ ) for all intervals of KH activity in this event, the ratio of the tetrahedron size to the KH wavelengths is between 0.11 and 0.23, where a linear dependence of magnetic curvature on tetrahedron size is expected (see K18). The average tetrahedron configuration has an elongation of  $0.07 \pm 0.05$  and planarity of  $0.08 \pm 0.04$ , which can be categorized as a regular tetrahedron where high accuracy of four-spacecraft tools are expected (Robert et al., 1998). Figure 2 shows average Cluster C1 (black), C2 (red), C3 (green), and C4 (blue) positions projected on GSM  $X$ - $Y$ ,  $X$ - $Z$ , and  $Y$ - $Z$  planes. C3 is chosen as the reference spacecraft for its middle position along the  $X$  and  $Y$  directions which correspond to the wave propagation and perturbation directions, respectively, as seen in Figure 2.

The magnetic curvature,  $\mathbf{C}$ , is calculated using the MCA derived by Shen et al. (2003) which applies a linear gradient estimation (e.g., Harvey, 1998) to calculate  $\mathbf{C} = \mathbf{b} \cdot \nabla \mathbf{b}$ , where  $\mathbf{b} = \mathbf{B}/|\mathbf{B}|$  is the average unit magnetic field at the tetrahedron barycenter. The magnetic curvature is estimated according to the expression  $C_j = B^{-2} B_i \nabla_i B_j - B^{-4} B_j B_i \nabla_i B_l$ , where  $\{i, j, k\}$  represent Cartesian coordinates  $(x, y, z)$ ,  $B_i = \sum_{\alpha=1}^4 B_{\alpha i}/4$  are the average magnetic field components, and  $\nabla_i B_j$  are the linear magnetic gradient tensors. Truncation errors of the method, arising from Taylor's expansion, are of order  $(a/D)^2$  where  $a$  is the spacecraft separation and  $D$  is the scale size of the resolved structure. The vorticity,  $\Omega = \nabla \times \mathbf{V}$ , where  $\mathbf{V}$  is the velocity field, is calculated using the linear barycentric estimator (Chanteur, 1998). The method calculates the curl of a velocity field according to  $\Omega = \sum_{\alpha=1}^4 \mathbf{k}_\alpha \times \mathbf{V}_\alpha$ , where  $\mathbf{k}_\alpha$  is the reciprocal vector and  $\mathbf{V}_\alpha$  is the ion bulk velocity of spacecraft- $\alpha$ . The reciprocal vector is derived from the relative spacecraft position vectors  $\mathbf{r}_{\alpha\beta} = \mathbf{r}_\beta - \mathbf{r}_\alpha$  according to  $\mathbf{k}_\alpha = (\mathbf{r}_{\beta\gamma} \times \mathbf{r}_{\beta\lambda}) / (\mathbf{r}_{\beta\alpha} \cdot \mathbf{r}_{\beta\gamma} \times \mathbf{r}_{\beta\lambda})$ , where  $(\alpha, \beta, \gamma, \lambda)$  is a cyclic permutation of  $(1, 2, 3, 4)$ . These two techniques have been applied on KH waves in 2.5-D magnetohydrodynamic simulations using varying tetrahedron sizes in K18.

Since the ion bulk velocity data are not available at C2, we require a proxy to apply the vorticity technique. We are interested in comparison with previously simulated fluid-scale bulk flow properties. We can use the results obtained from applying a three-spacecraft technique on ion data (Shen et al., 2012) to corroborate our derived vorticity. The high-cadence C2 electron data set would require a separate treatment (F08). We thus obtain a proxy for the C2 ion bulk velocity by considering the 3-D spacecraft configuration in Figure 2 with respect to wave perturbations as follows. KH waves are mainly confined in the equatorial plane ( $X$ - $Y$  plane in GSM system or  $M$ - $N$  in LMN system) when the IMF is strongly northward. The waves propagate tailward in  $-X$  direction ( $-M$  in LMN system) with their amplitude growing in  $Y$  direction ( $N$  in LMN system; see also Figure 1). C2 and C3 are far apart in the  $Z$  direction as seen in Figures 2b and 2c by about  $0.3 R_E$ , but this direction should not be of concern for our proposed approximation because it is not the main perturbation direction. Given that C2 is located close to C3 in the  $X$  direction by about  $0.1 R_E$  and at almost the same level in the  $Y$  direction as seen in Figure 2a, we obtain the C2 ion bulk velocity proxy by time shifting the C3 ion bulk velocity data with time delays obtained from cross correlation between time series. These time delays

**Table 1**

Time Lags Between C2 and C3 From Table 4 of F08 From Magnetic Field Component  $B_m$  and Electron Temperature Component  $T_{e\perp}$  for (a) Inbound and (b) Outbound Crossings

Intervals	(a) $B_{m3} - B_{m2}$	(b) $B_{m3} - B_{m2}$	(a) $T_{e\perp3} - T_{e\perp2}$	(b) $T_{e\perp3} - T_{e\perp2}$	Average
A	20.4 s	-3.0 s	10.6 s	-1.5 s	6.6 s
B	8.1 s	20.3 s	9.6 s	4.8 s	10.7 s
C	—	—	11.1 s	18.7 s	14.9 s
D	17.6 s	8.8 s	4.1 s	10.5 s	10.3 s
E	-17.4 s	—	—	22.0 s	2.3 s

were derived by F08 (see their Table 4), where they obtain average four-spacecraft timings at C1–C4 from magnetic field component  $B_m$  and electron perpendicular temperature  $T_{e\perp}$  time series for both inbound and outbound crossings. These time delays are shown in Table 1 for (a) inbound and (b) outbound crossings for both  $B_m$  and  $T_{e\perp}$  for the five intervals characterized in F08. We use the average of these time delays in each 2-hr interval. Averaging both time lags from magnetic field and temperature series gives better statistics for ion velocity. Above considerations are based on the stationarity assumption of the waveform in the time scale of the time lags between C2 and C3. The stationarity assumption is valid when the time lags are much shorter than the KH development time. Comparing the average time lags of all cases of 2 to 15 s (Table 1) to relevant KH wave periods of 3 to 4 min and derived properties over intervals of 12 min and 2 hr in section 3.3, the stationarity assumption is acceptable. Our vorticity result using the synthetic C2 ion velocity is found to be consistent with the vorticity calculated using a three-spacecraft technique by Shen et al. (2012) for the same interval.

### 3. Results

#### 3.1. Magnetic Curvature in the Magnetopause Boundary Layers Disturbed by KH Waves

We first examine the magnetic curvature in the boundary layers disturbed by KH waves in order to investigate magnetic field distortions in the presence of the KH instability. Figure 3 shows time series between 15:39 and 15:46 UT for two adjacent waveform crossings: first, numbers (1)–(4), and second, numbers (1′)–(4′) marked by vertical black lines. The first waveform crossing between 15:39 and 15:43 UT (numbers (1) to (4)) is shown as an example of an oscillatory structure in F08. This time interval is part of interval B which has the lowest clock angle ( $12^\circ \pm 10^\circ$  among the five intervals A–E).

Figure 3a shows ion density at C1 (black) and C3 (green) which refer roughly to inner (tenuous) and outer (dense) magnetospheric boundary layers. Since the KH waves propagate tailward, we may refer to transitions between boundary layer regions seen by the spacecraft as follows. An “outbound” transition is associated with the trailing edge (sunward facing edge; see Figure 1a) of the wave where the spacecraft transits from the inner to outer magnetospheric boundary layers, for example, from (1) to (2) and (1′) to (2′). An “inbound” transition is associated with the leading edge of the wave where the spacecraft transits from the outer to inner magnetospheric boundary layers, for example, from (3) to (4) and from (3′) to (4′). Figure 3b shows magnetic field components at C3 with magnetic field rotations during the inbound and outbound transitions, best seen in  $B_m$  (purple line). These are signatures seen by all spacecraft.

We are next considering magnetic curvature at the barycenter of the four Cluster spacecraft as resolved by MCA. Figure 3c shows curvature components which indicate the direction of the magnetic tension force perpendicular to the magnetic field lines (see Figure 1c). Curvature component  $C_m$  (purple) changes from positive (approximately sunward) to negative (approximately tailward) values during the outbound crossings, while it changes from negative to positive values during the inbound crossings. Figure 3d shows radius of curvature (see Figure 1d) defined by  $R_c = 1/\sqrt{C_l^2 + C_m^2 + C_n^2}$  with a truncation error  $(a/R_c)^2$  where  $a$  is the tetrahedron size. The radius of curvature typically reaches a local minimum at each marked number (vertical solid line). Considering magnetic field configuration in the equatorial plane, we consider a 2-D curvature projection  $\mathbf{C}_p = C_m \mathbf{m} + C_n \mathbf{n}$ . Figure 3e shows the 2-D normalized curvature projection vectors with color-coded angles  $\theta = \arctan(C_n/C_m)$  (consistent with those in Figure 1a). The curvature projection changes from sunward (mint green) at around (1) to tailward (red) at around (2) during the outbound crossing. The curvature projection changes from tailward and earthward (purple) at around (3) to the opposite direction (green) at around (4) during the inbound crossing. These observational results show that magnetic

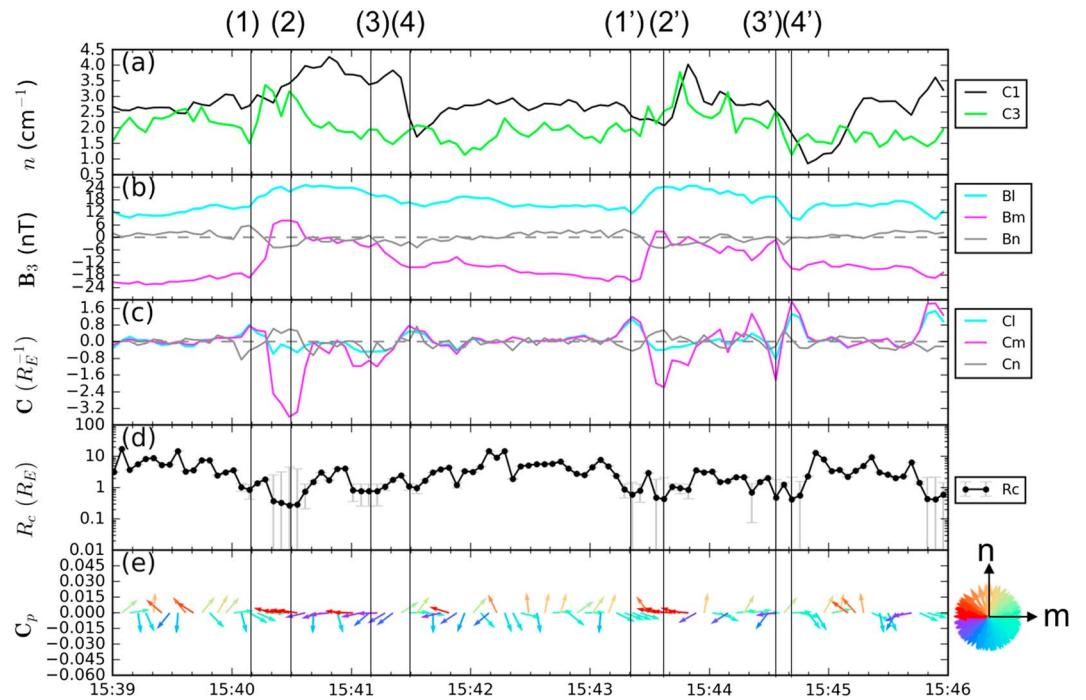


**Figure 3.** Crossings of an oscillatory structure between 15:39 and 15:46 UT. (a) Ion density at C1 and C3, (b) magnetic fields at C3, (c) magnetic curvature components, (d) radius of curvature, and (e) 2-D normalized curvature projection  $C_p = (C_m \mathbf{m} + C_n \mathbf{n}) / \sqrt{C_m^2 + C_n^2}$  with a color-coded angle  $\arctan(C_n/C_m)$ .

curvature points in opposite directions when crossing the boundary layers disturbed by the KH waves, confirming the simulation result in K18.

The opposite change of curvature direction across the boundary layer is likely due to the bending of magnetic fields by the KH waves. We notice that the magnetic field rotation at outbound crossings (e.g., from (1) to (2)) is more pronounced than that at the inbound crossings (e.g., from (3) to (4)). Also, we notice that the radius of curvature in Figure 3d on the outer magnetospheric side (e.g., number (2)) is smaller than that on the inner magnetospheric side (e.g., number (1)). This implies that the magnetic field bending is stronger on the outer magnetospheric side.

### 3.2. Rolled-up Vortex Signatures

Figure 4 shows time series for the interval between 20:30 and 20:40 UT. This time interval was shown to have signatures consistent with rolled-up vortices in Hasegawa et al. (2004, 2006). This time interval is also studied in the wider 2-hr interval D by F08 and used for illustrations of three-spacecraft calculations of vorticity and current density in Shen et al. (2012). We are now revisiting this time interval using the four-spacecraft techniques described in section 2.

Figures 4a–4d) show time series from C1, C2, C3, and C4, with black, red, green, and blue lines, respectively. Vertical dotted lines mark outbound transitions in which the spacecraft transit from inner to outer magnetospheric boundary layers (wave trailing edges). Figure 4a shows magnetic field components  $B_m$ , which generally increases sharply at each outbound transition. Figure 4b shows ion density which also generally increases sharply at the outbound transitions. Figure 4c shows ion bulk velocity components  $V_m$  (thick solid lines) and  $V_n$  (thin solid lines) with the proxy data at C2. Using the lower-density and faster-than-sheath (LDFTS) criteria given in Hasegawa et al. (2006) where  $n < 6 \text{ cm}^{-3}$  and, to first approximation,  $|V_m| > 290 \text{ km/s}$ , we mark the ion population that fits the criteria in Figure 4b with green dots. The LDFTS population is best seen at  $\sim 20:33 \text{ UT}$  marked by a vertical black solid line, colocated with the fast tailward speed ( $V_m < -290 \text{ km/s}$ ) in Figure 4c (thick solid lines). This population is found at the beginning of a turning of the ion bulk velocity component  $V_n$  from earthward ( $V_n < 0$ ) to anti-earthward ( $V_n > 0$ ) seen at C1 (black thin line) which corresponds to a counterclockwise (CCW) vortical flow seen from above the equatorial plane, as expected for vortices developed on the duskside. These are strong evidence of a vortex.

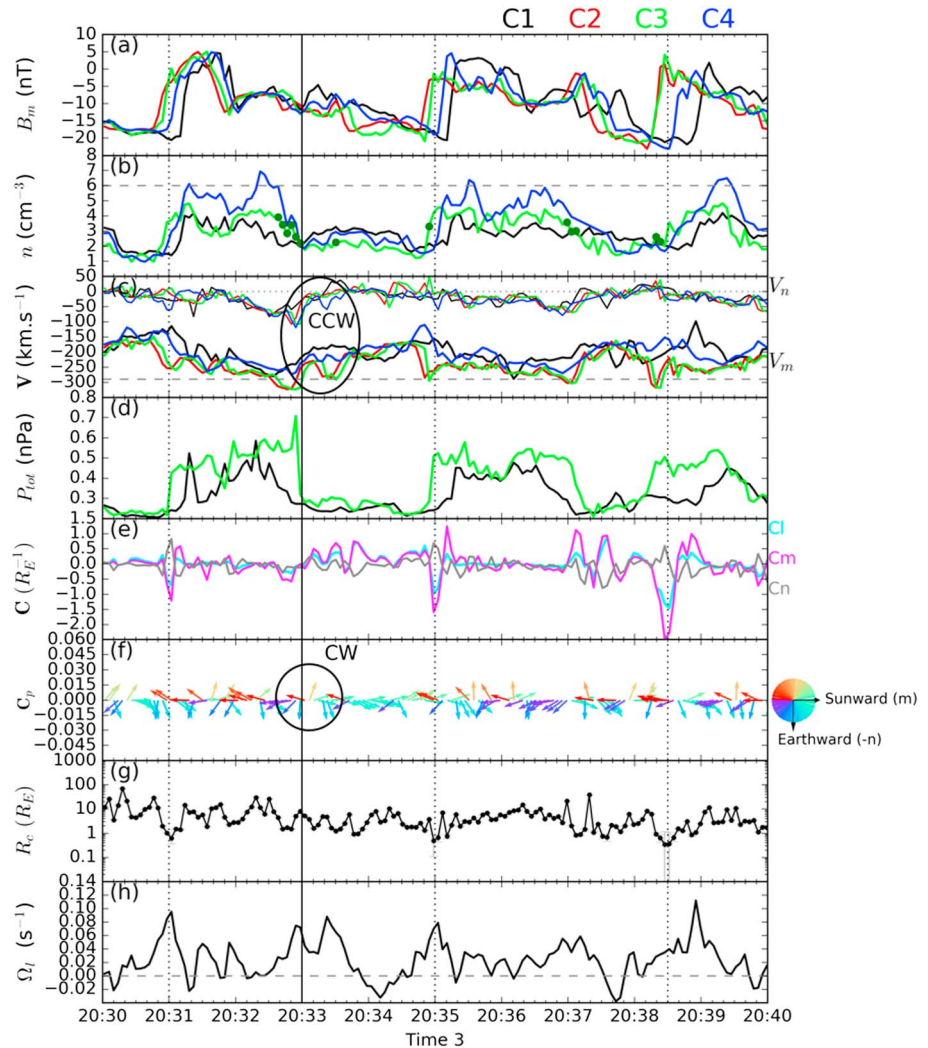


**Figure 4.** Time series observed on 20 November 2001 during 20:30 and 20:40 UT at C1 (black), C2 (red), C3 (green), and C4 (blue) of (a) magnetic field component  $B_m$ , (b) ion density  $n$ , (c) ion velocity components  $V_m$ ,  $V_n$ , and (d) total pressure  $P_{\text{tot}}$ . Four-spacecraft results at the tetrahedron barycenter—(e) magnetic curvature components  $C_l$ ,  $C_m$ ,  $C_n$ , (f) 2-D normalized curvature projection  $C_p = (C_m \mathbf{m} + C_n \mathbf{n}) / \sqrt{C_m^2 + C_n^2}$  with a color-coded angle  $\arctan(C_n/C_m)$ , (g) curvature radius  $R_c$ , and (h) northward component,  $\Omega_l$ , of the vorticity ( $\Omega = \Omega_l \mathbf{l} + \Omega_m \mathbf{m} + \Omega_n \mathbf{n}$ ).

Figure 4d shows total pressure of magnetic and kinetic pressure which is typically high at outbound transitions and low in the vicinity of vortex centers, as expected from simulations.

The MCA results are shown in Figures 4e–4g. Figure 4e shows curvature components and Figure 4f shows the normalized curvature projection ( $C_p = C_m \mathbf{m} + C_n \mathbf{n}$ ). The outbound transitions (vertical dotted lines) collocate with  $C_m$  minima in the outer magnetospheric side, which correspond to tailward curvature ( $C_m < 0$ ) in Figure 4e (purple line). In Figure 4f, we notice a curvature vector rotation at around 20:33 UT marked by a circle next to the LDFTS plasma (green dots in Figure 4b). The curvature projection rotates from tailward (red) to sunward (mint green), corresponding to a clockwise (CW) rotation seen from above the equatorial plane, and consistent with the curvature directions sketched in Figure 1a at the vortex center. This curvature rotation is against the CCW vortical flow at 20:33 UT, reported earlier in Figure 4c. During 20:33 and 20:35 UT, the curvature vectors mainly point in sunward and earthward direction (mint green). Figure 4g shows the radius of curvature, which is typically found to reach a local minimum at the outbound transitions (similar to (2) and (2') in Figure 3d). The radius of curvature does not show distinct variations during the rolled-up vortex passage at 20:33 UT.

**Table 2**

*Upstream and Local Parameters for the Five Intervals A–E With Statistical Standard Deviations: IMF Clock Angle (CA), Solar Wind Proton Bulk Speed ( $V_{sw}$ ), Proton Density ( $\rho_{sw}$ ), Average Minimum Radius of Curvature ( $R_{c,min}$ ) in  $R_E$ , Average Maximum Vorticity ( $\Omega_{l,max}$ ), and Average Minimum Vorticity ( $\Omega_{l,min}$ )*

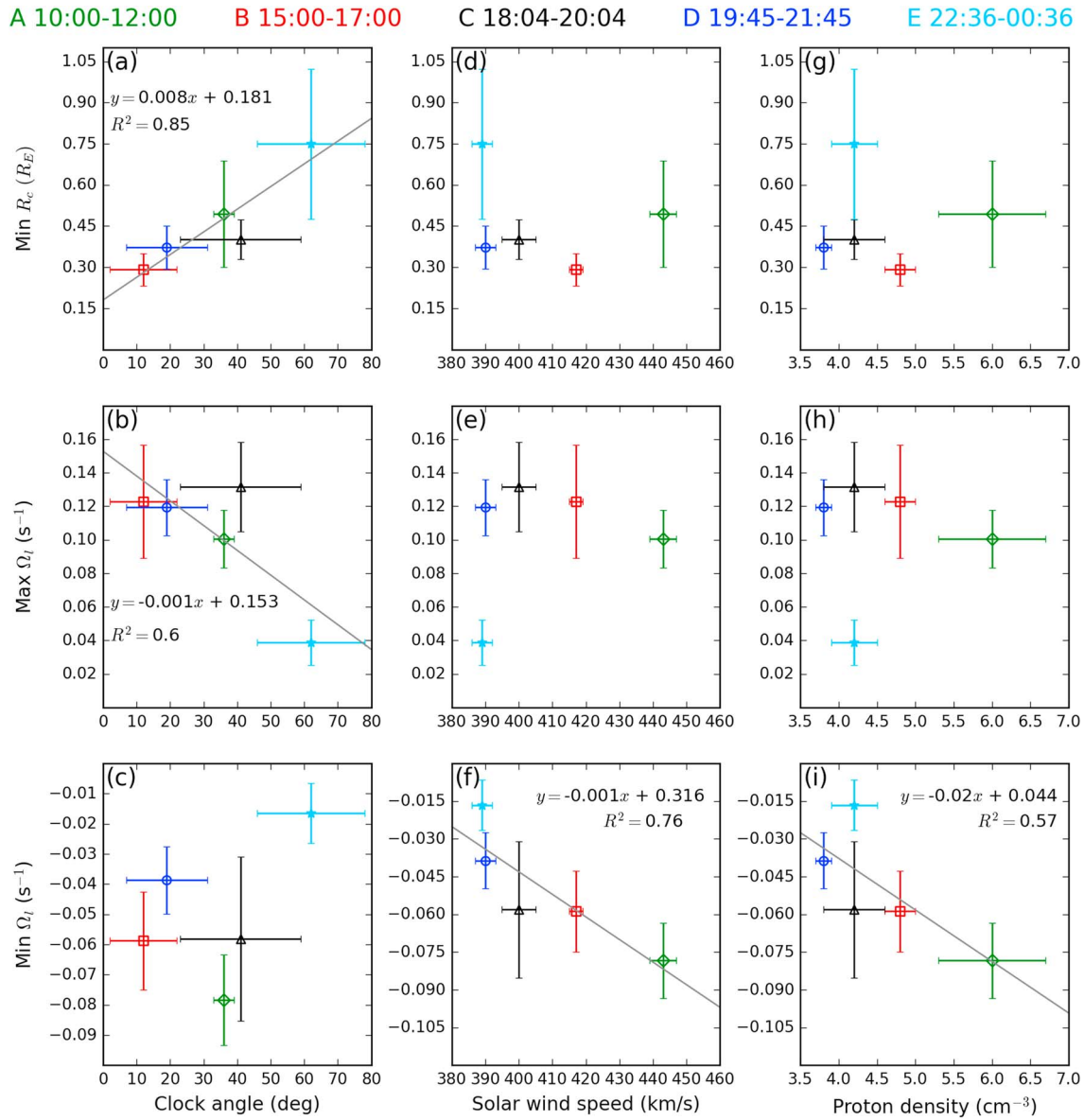
Intervals	CA (°)	$V_{sw}$ (km/s)	$\rho_{sw}$ ( $\text{cm}^{-3}$ )	$R_{c,min}$ ( $R_E$ )	$\Omega_{l,max}$ ( $\text{s}^{-1}$ )	$\Omega_{l,min}$ ( $\text{s}^{-1}$ )
A	$36 \pm 3$	$443 \pm 4$	$6.0 \pm 0.7$	$0.50 \pm 0.19$	$0.101 \pm 0.017$	$-0.078 \pm 0.015$
B	$12 \pm 10$	$417 \pm 2$	$4.8 \pm 0.2$	$0.29 \pm 0.06$	$0.123 \pm 0.034$	$-0.059 \pm 0.016$
C	$41 \pm 18$	$400 \pm 5$	$4.2 \pm 0.4$	$0.40 \pm 0.07$	$0.129 \pm 0.030$	$-0.058 \pm 0.027$
D	$19 \pm 12$	$390 \pm 3$	$3.8 \pm 0.1$	$0.37 \pm 0.08$	$0.119 \pm 0.017$	$-0.039 \pm 0.011$
E	$62 \pm 16$	$389 \pm 3$	$4.2 \pm 0.3$	$0.75 \pm 0.27$	$0.038 \pm 0.013$	$-0.017 \pm 0.001$

Figure 4h shows northward vorticity component  $\Omega_l$ , which is along  $Z$  in GSM coordinates. The northward vorticity is found to reach a maximum at the outbound transitions, consistent with the three-spacecraft study by Shen et al. (2003). These maxima are due to the shear layer transitions at the wave trailing edges (see Figure 1b), typically associated with high total pressure, and should not be confounded with vortex centers which correspond to low total pressure. For the rolled-up vortex at around 20:33 UT, we notice high positive vorticity interval with a peak of value  $\Omega_l \sim 0.10 \text{ s}^{-1}$ . After that, the vorticity decreases and then reaches negative values with a minimum of  $-0.03 \text{ s}^{-1}$  at around 20:34 UT. This pair of high positive and small negative vorticity intervals confirm the rolled-up vortex signature found in the simulation by K18 as sketched in Figure 1b. The negative vorticity is also found in the next adjacent waveform with more negative values briefly before 20:38 UT, consistent with the simulation result that the negative vorticity remains present in the saturation phase.

### 3.3. Parametric Survey

We further apply the four-spacecraft techniques in the intervals A–E to compare properties of local magnetic and flow structures when the wave activity is subjected to different solar wind conditions (as characterized in F08). For the magnetic curvature property, we consider a minimum curvature, which is typically found at the wave trailing edges (e.g., vertical dotted lines in Figure 4g). Note that a maximum curvature radius is of no interest because it is typically very large and therefore indicates a straight magnetic field line. For the vorticity, we consider its maximum and minimum values. These curvature radius and vorticity extrema may be regarded as the local properties associated with the waves. To obtain these extrema, we divide each 2-hr interval into 10 subintervals of 12 min. The chosen subinterval duration is larger than the KH wave period which is 3–4 min for the dominant mode (see Table 5 of F08) and is adequate because a waveform does not always periodically appear. The extrema are obtained for each subinterval and their averages for each 2-hr interval are presented in Table 2. We follow the characterized 2-hr intervals in F08 as they provide optimal intervals to study a variety of solar wind IMF clock angle conditions and minimize standard deviations of the IMF clock angles.

The representative four-spacecraft outputs are plotted against the solar wind conditions in Figure 5. The upper panels, Figures 5a, 5d, and 5g, show the average minimum radius of curvature against the solar wind conditions. The minimum radius of curvature positively correlates with IMF clock angle as seen in Figure 5a. This means that magnetic field structures are more bent (smaller radius of curvature) for lower IMF clock angle. The minimum radius of curvature does not show significant correlations with either solar wind speed (Figure 5d) or proton density (Figure 5g). The middle panels, Figures 5b, 5e, and 5h, show the average maximum vorticity against the solar wind conditions. The maximum vorticity has a positive sign as expected for vortices developed on the duskside magnetopause. The maximum vorticity is found to be higher for lower IMF clock angle as seen in Figure 5b. Excluding the interval E, the maximum vorticity slightly decreases with faster solar wind speed as seen in Figure 5e and denser proton density as seen in Figure 5h. Note the interval E has almost no KH activity and therefore may be regarded as a control group. In addition, one can see that the interval C has the highest maximum vorticity in Figure 5b. From detailed investigations, it appears that there is a sudden drop in ion bulk velocity, for about  $\Delta V = 250 \text{ km/s}$  during the interval C (see Figure 2b of F08 for data at C3). Therefore, the high vorticity of the interval C is not purely caused by the KH wave activity but results from the sudden change in ion bulk velocity during the interval (hence, the large error bar). The lower panels, Figures 5c, 5f, and 5i, show the average minimum vorticity against the solar wind conditions. The minimum vorticity has a negative sign. The minimum vorticity does not well correlate



**Figure 5.** Parameter space plots between upstream parameters (a–c) IMF clock angle, (d–f) solar wind proton bulk speed, (g–i) solar wind proton density versus in situ four-spacecraft outputs (a,d,g) minimum radius of curvature, (b,e,h) maximum vorticity, and (c,f,i) minimum vorticity for the five intervals A (green diamond), B (red square), C (black triangle), D (blue circle), and E (cyan star) with average values and standard deviations shown in Table 2.

with the IMF clock angle as seen in Figure 5c. The minimum vorticity becomes more negative with the higher solar wind speed as seen in Figure 5f and higher proton density as seen in Figure 5i. Despite limited data points, Figures 5a, 5b, 5f, and 5i show good correlations (with the correlation coefficient  $R^2 \geq 0.6$ ). We discuss all these features in the next section.

#### 4. Discussions

The four-spacecraft analyses above have revealed additional signatures of the KH waves observed on 20–21 November 2001 by Cluster, complementary to previous analyses. MCA reveals magnetic distortions caused by the KH waves. In particular, we have seen evidence of magnetic field twisting against the vortical flow at the vortex center (highlighted by black circles in Figures 4c and 4f), consistent with the simulation in K18 (Figure 1a). MCA also aids in distinguishing KH waves regions as proposed in K18, by confirming several signatures as follows. First, we find minimum curvature radii at the wave trailing edges (less than  $1 R_E$ ). Second, in the same regions, magnetic curvature, which points in the magnetic tension direction, is

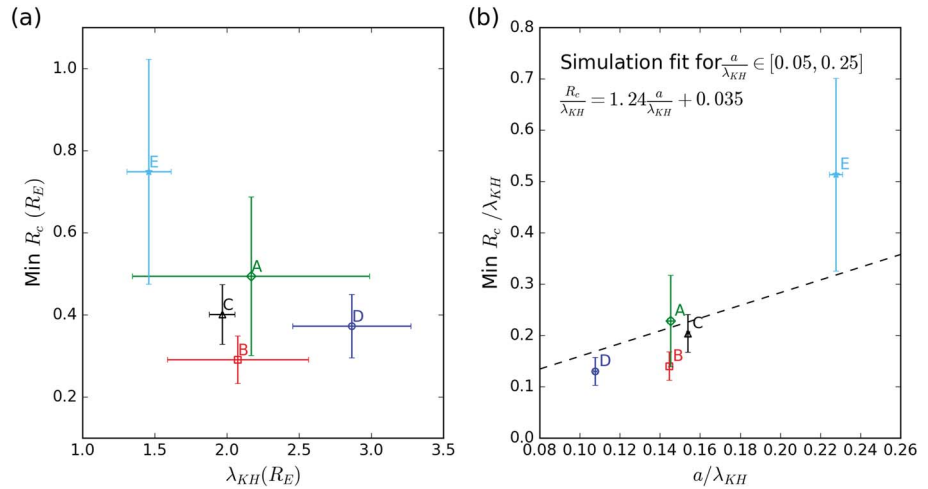


**Figure 6.** (a) Minimum curvature radii versus Kelvin-Helmholtz (KH) wavelengths of the dominant modes in the five intervals A–E. (b) Minimum curvature radii versus Cluster tetrahedron sizes, both of which in KH wavelength unit. Dashed line in panel (b) is a linear fit of the curvature radii in the KH wave trailing edge with the varying tetrahedron sizes in the simulation by K18.

found to point sunward and earthward on the inner magnetospheric side and to rotate into the opposite direction on the outer magnetospheric side. This magnetic field distortion at the wave trailing edges may be favorable for magnetic reconnection, the so-called Type I vortex-induced-reconnection (e.g., Nakamura & Fujimoto, 2008), and it is consistent with recent observations (Eriksson et al., 2016). Evidence of magnetic reconnection is reported at 20:34:55 UT (near the third vertical dashed line in Figure 4) by Hasegawa et al. (2009). Magnetic field distortions due to the twisting of the magnetic field lines may lead to the antiparallel magnetic configuration (in 3-D) favorable for reconnection at this location.

We have shown signatures of vorticity as seen in Figure 4h between 20:31 and 20:35 UT, consistent with rolled-up vortices and rolled-up history proposed by K18 (Figure 1b). A relatively high positive vorticity is found in the vicinity of the LDFTS plasma as seen in Figure 4b and 4h. We note here that the magnitude of the vorticity at the vortex center is not significantly higher than that at the boundary layer (original shear layer). In K18 (and also in Gratton et al., 2009), the vortex center has stronger vorticity than that of the original shear layer. This is possibly because the detected KH waves are at the interface between outer and inner magnetospheric boundary layers, while those in the simulations are at the magnetopause surface. We also found negative vorticity next to the positive vorticity at the vortex center, consistent with simulations in K18 (see Figure 1b). This feature is also consistent with counterrotating vortices (with the negative vorticity), which arises after one roll-over time shown in three-dimensional magnetohydrodynamic simulations by Gratton et al. (2009).

We now discuss the features identified in Figure 5 from comparing the five 2-hr data intervals characterized by F08. Since F08 demonstrated the occurrence of larger KH wavelength and amplitude for lower IMF clock angle, it is possible to discuss relationships between the size of the KH waves and the local properties given by our results. In Figure 6, we choose to show relationships between the minimum curvature radius and the KH wavelength; the relationships for the maximum vorticity will be similar but with a reversed trend (not shown). Average minimum curvature radii versus KH wavelengths of the dominant modes for the five intervals are plotted in Figure 6a. There is a tendency for the smaller (minimum) curvature radius measurement to occur in larger KH waves. This could result from nonlinear developments of small-scale structures inside the large-scale waves. However, taking into account the tetrahedron size effect in Figure 6b, we reveal a dependence that can be interpreted as multiscale structures resolved by different ratios of  $a / \lambda_{KH}$ .

Consistent with nonlinear spatial variations of physical structures, K18 found that the magnetic curvature radius measurement resolved by MCA is dependent on the tetrahedron size. These nonlinear spatial variations can be resolved by a cross-scale configuration of small- and larger-scale tetrahedrons with the same barycenter, as shown in their simulation for a single wavelength KH wave. Looking for such observational evidence, we have used for the first time a favorable event to resolve spatial variations of the magnetic

structures in multiscales, thanks to variations in KH wavelengths for five intervals with approximately fixed tetrahedron size (opposite to K18's case). To examine this, Figure 6b shows the measurements of minimum curvature radii against the tetrahedron sizes relative to the wavelength for the five intervals. The ratio of the minimum curvature radius to the wavelength is roughly increasing with the ratio of the tetrahedron size to the wavelength  $a/\lambda_{KH}$ . This shows that the minimum curvature radius measure is increasing with the relative tetrahedron size. The dashed black line represents a linear fit to revised numerical data (published in K18, revised in Kieokaew, 2019, to correct for a small numerical inaccuracy) for curvature radii in the wave trailing edge, where the minimum curvature radius is typically found, resolved by the varying tetrahedron sizes, viz.

$$R_c/\lambda_{KH} = 1.24a/\lambda_{KH} + 0.035 \quad (1)$$

for their range  $a/\lambda_{KH} \in [0.05, 0.25]$  where the linear dependence on the tetrahedron size is found. The data points from Cluster are roughly consistent with the linear fit from the simulation, which confirms the dependence of the curvature radius measure on the (relative) tetrahedron size. This plot illustrates the nonlinearity of spatial variations of the magnetic field structures in observations as resolved by Cluster.

The above comparison with the simulation assumed that the KH waves in the five intervals for this event have spatial variations governed essentially by their amplitudes (or wavelengths) and/or physical parameters (density, velocity jumps) controlling the KHI excitation. This is not entirely true as these waves can have other, possibly minor, spatial variations due to their nonlinear evolution (rolled-up vortex signatures and other nonlinear spatial variations). These waves are considered to be of remote origin [F08] such that they are produced somewhere on the dayside where the conditions are KH-unstable (Farrugia et al., 1998), for example, where the shear angle between the IMF clock angle and the Earth's magnetic fields is low, and so the waves in the five intervals of different IMF clock angles have different growth rates at the source regions. Consequently, these waves are in different stages of development when they are probed by Cluster. Of particular relevance is the simulation result (for fixed wavelength) that the average radius of magnetic curvature can become smaller when the KH wave evolves from linear to nonlinear stages (Kieokaew et al., 2018; Ryu et al., 2000). Since the intervals A (IMF clock angle =  $36^\circ \pm 3^\circ$ ,  $\lambda_{KH} = 2.16 \pm 0.82 R_E$ ) and B (IMF clock angle =  $12^\circ \pm 10^\circ$ ,  $\lambda_{KH} = 2.07 \pm 0.49 R_E$ ) in Figure 6b have the same ratios of  $a/\lambda_{KH}$ , we can attribute the differences to the impact of nonlinear KH development on the radius of curvature. Here, the KH waves in interval B have smaller minimum  $R_c/\lambda_{KH}$  than that of the interval A. This is consistent with the other properties showing that the KH waves in the interval B are more developed than the waves in the interval A (F08).

Higher (maximum) positive vorticity in longer wavelength KH waves (not shown) is consistent with larger vortices found in KH simulations of the magnetopause (e.g., Belmont & Chanteur, 1989; Miura, 1999). In addition to the main positive vorticity expected on the duskside, we have found the negative vorticity which is a secondary feature associated with rolled-up vortices (consistent with Figure 1b). In theory, negative vorticity occurs after rolling up (Gratton et al., 2009), and we would expect the negative vorticity layer between the positive vorticity layers of a rolled-up vortex core and an original shear layer (K18). However, from the observations (F08), we know that not all five intervals contain rolled-up vortex signatures. Indeed, in interval E, the method picks up vorticity minima that are close to zero (see Figures 5c, 5f, and 5i), but still negative. This interval contains little wave activity and therefore should not be regarded as having any rolled-up vortex signature. The strength of the negative vorticity increases with the solar wind speed (Figure 5f), consistent with more developed KH waves as expected for higher velocity shear across the boundary layer. In addition, the magnitude of the (positive, negative) vorticity should be initially controlled by the vorticity scaling value  $|\Omega| \sim |V_{sw}/\Delta L|$ , where  $V_{sw}$  is the solar wind speed and  $\Delta L$  is the thickness of the boundary layer (e.g., K18); the KH activity then amplifies/weakens this initial vorticity. Using the boundary layer thickness ( $\Delta L$ ) obtained by F08 in their Table 3, it can be shown that the scaling values of all intervals are in the order  $A > C > B > D > E$  that is in the same order as the negative vorticity in Figure 5f. The relationship between the negative vorticity and the proton density (panel (i)) is consistent with simulation results in Nakamura et al. (2004). There, the negative vorticity (referred as a reversed shear flow) only occurs when there is a density jump across the shear layer. Since the density jump is modified by proton density on the magnetosheath side, the negative vorticity development is associated with solar wind proton density. This is confirmed by our result in Figure 5i as one can see that the negative vorticity tends to zero for lower proton density.

## 5. Summary

Observations of KH waves on 20–21 November 2001 made by Cluster are revisited using the four-spacecraft magnetic curvature and vorticity analyses. Several four-spacecraft signatures in magnetic curvature and flow vorticity of KH waves proposed by K18 are confirmed. We observe a rotation of curvature direction from sunward and earthward in the inner magnetospheric side to the opposite direction in the outer magnetospheric side across the wave trailing edges, consistent with K18. Rolled-up vortex signatures are further highlighted by the four-spacecraft tools complementary to previous studies using single-spacecraft observations. We observe the magnetic field distortion against the vortical flow at the vortex center. We also observe the negative vorticity layer adjacent to the positive vorticity of the vortex core of a rolled-up KH vortex where the LDFTS plasma is found. The confirmation of such vorticity variations is useful to assess whether identifying rolled-up KH waves in four-spacecraft observations may be applicable. Local properties of the KH waves are characterized with changes in solar wind conditions. In particular, we found the smaller radius of magnetic curvature (stronger bending) and larger positive flow vorticity for lower IMF clock angle (longer wavelength KH waves). The average minimum curvature radii are compared for various ratios of the tetrahedron size to the wavelength. We have demonstrated observationally the dependence of the curvature radius measurement on the tetrahedron size, consistent with nonlinear spatial variations of magnetic structures resolved by nested cross-scale virtual spacecraft tetrahedrons in a numerical simulation. Finally, we confirm the importance of local conditions on the development of the negative vorticity as previously found in the simulations, such that the negative vorticity is associated with the density jump and strengthened with higher solar wind proton density. We additionally find that it also strengthens with increasing solar wind speed. In other words, there are three possible effects that are being detected in the parametric study in the various panels of Figure 5. The first one observed as linear relationships as seen in Figures 5a and 5b could be caused by the scale size of the KH waves (controlled by the IMF clock angle) with respect to the tetrahedron size. The impact of the  $a/\lambda_{KH}$  ratio is summarized in Figure 6 (shown for the minimum curvature radius). The second effect also observed as linear relationships in Figures 5f and 5i could be due to the physical parameters that control the KHI excitation, for example, density and velocity jumps across the shear interface or the vorticity scaling that is a characteristic of the boundary layer (associated speed and layer thickness). The third effect observed in the lack of linear relationship could be attributed to nonlinear KH evolution. The negative vorticity (e.g., Figure 5c) is one of the spatial variations expected to arise due to nonlinear KH evolution. However, not all negative vorticity in the data can be taken as a signature of rolled-up vortices, and there is no evidence that the strongest negative vorticity occurs in relation to nonlinear KH evolution either. Further investigations to understand the development of negative vorticity would be needed, for example, using the KH vortex frame in observational data, but they are beyond the scope of this study. While more data points are desirable for better statistics in the parametric survey, we cannot conduct an ideal “controlled” experiment with unrelated KH events that may resemble in some aspects our selected event, but will always differ in solar wind/local plasma conditions and satellite relative locations and separations. The multiscale analysis in this work has broad applications especially for cross-scale observations of complex magnetic and vortical flow structures, which are ubiquitous in the Earth’s magnetospheric environments.

## Acknowledgments

R. K. acknowledges financial support from the College of Engineering, Mathematics, and Physical Sciences (CEMPS) at the University of Exeter. C. F. acknowledges financial support from the UK Science and Technology Facilities Council (STFC) under her Advanced Fellowship ST/I003649. We are thankful for the data used in this study, which are obtained from CLWeb at IRAP (<http://clweb.irap.omp.eu/cl/clweb.php>).

## References

- Belmont, G., & Chanteur, G. (1989). Advances in magnetopause Kelvin-Helmholtz instability studies. *Physica Scripta*, *40*(40), 124–128.
- Chanteur, G. (1998). Spatial interpolation for four spacecraft: Theory. *ISSI Scientific Report Series*, *1*, 349–370.
- Chaston, C. C., Wilber, M., Mozer, F. S., Fujimoto, M., Goldstein, M. L., Acuna, M., et al. (2007). Mode conversion and anomalous transport in Kelvin-Helmholtz vortices and kinetic Alfvén waves at the earth’s magnetopause. *Physical Review Letters*, *99*(17), 175004. <https://doi.org/10.1103/PhysRevLett.99.175004>
- Eriksson, S., Lavraud, B., Wilder, F. D., Stawarz, J. E., Giles, B. L., Burch, J. L., et al. (2016). Magnetospheric multiscale observations of magnetic reconnection associated with Kelvin-Helmholtz waves. *Geophysical Research Letters*, *43*, 5606–5615. <https://doi.org/10.1002/2016GL068783>
- Escoubet, C., Fehringer, M., & Goldstein, M. (2001). The Cluster mission. *Annales Geophysicae*, *19*, 1197–1200. <https://doi.org/10.5194/angeo-19-1197-2001>
- Farrugia, C. J., Gratton, F. T., Bender, L., Biernat, H. K., Erkaev, N. V., Quinn, J. M., et al. (1998). Charts of joint Kelvin-Helmholtz and Rayleigh-Taylor instabilities at the dayside magnetopause for strongly northward interplanetary magnetic field. *Journal of Geophysical Research*, *103*(A4), 6703. <https://doi.org/10.1029/97JA03248>
- Foullon, C., Farrugia, C., Fazakerley, A., Owen, C., Gratton, F., & Torbert, R. (2008). Evolution of Kelvin-Helmholtz activity on the dusk flank magnetopause. *Journal of Geophysical Research*, *113*, A11203. <https://doi.org/10.1029/2008JA013175>
- Foullon, C., Farrugia, C., Fazakerley, A., Owen, C., Gratton, F., & Torbert, R. (2010). On the multispacecraft determination of periodic surface wave phase speeds and wavelengths. *Journal of Geophysical Research*, *115*, A09203. <https://doi.org/10.1029/2009JA015189>

- Foullon, C., Verwichte, E., Nakariakov, V. M., Nykyri, K., & Farrugia, C. J. (2011). Magnetic Kelvin-Helmholtz instability at the Sun. *The Astrophysical Journal Letters*, 729(1 PART II), 2–5. <https://doi.org/10.1088/2041-8205/729/1/L8>
- Graton, F. T., Bilbao, L. E., Farrugia, C. J., & Gnani, G. (2009). Large eddy simulations in MHD: The rise of counter-rotating vortices at the magnetopause. *Journal of Physics: Conference Series*, 166, 12023. <https://doi.org/10.1088/1742-6596/166/1/012023>
- Harvey, C. (1998). Spatial gradients and the volumetric tensor. *ISSI Scientific Report Series*, 1, 307–322.
- Hasegawa, H., Fujimoto, M., Phan, T.-D., Rème, H., Balogh, A., Dunlop, M., et al. (2004). Transport of solar wind into Earth's magnetosphere through rolled-up Kelvin-Helmholtz vortices. *Nature*, 430, 755–758. <https://doi.org/10.1038/nature02799>
- Hasegawa, H., Fujimoto, M., Takagi, K., Saito, Y., Mukai, T., & Rème, H. (2006). Single-spacecraft detection of rolled-up Kelvin-Helmholtz vortices at the flank magnetopause. *Journal of Geophysical Research*, 111, A09203. <https://doi.org/10.1029/2006JA011728>
- Hasegawa, H., Retinó, A., Vaivads, A., Khotyaintsev, Y., André, M., Nakamura, T. K. M., et al. (2009). Kelvin-Helmholtz waves at the Earth's magnetopause: Multiscale development and associated reconnection. *Journal of Geophysical Research*, 114, A12207. <https://doi.org/10.1029/2009JA014042>
- Hillier, A., & Polito, V. (2018). Observations of the Kelvin-Helmholtz instability driven by dynamic motions in a solar prominence. *The Astrophysical Journal Letters*, 864, L10. <https://doi.org/10.3847/2041-8213/aad9a5>
- Kieokaew, R. (2019). Multi-scale structure analyses of magnetopause Kelvin-Helmholtz waves: applications of four-spacecraft to MHD simulations and Cluster and MMS observations. (Ph.D. thesis). University of Exeter.
- Kieokaew, R., Foullon, C., & Lavraud, B. (2018). Four-spacecraft magnetic curvature and vorticity analyses on Kelvin-Helmholtz waves in MHD simulations. *Journal of Geophysical Research: Space Physics*, 123, 513–529. <https://doi.org/10.1002/2017JA024424>
- Masters, A., Achilleos, N., Kivelson, M. G., Sergis, N., Dougherty, M. K., Thomsen, M. F., et al. (2010). Cassini observations of a Kelvin-Helmholtz vortex in Saturn's outer magnetosphere. *Journal of Geophysical Research*, 115, A07225. <https://doi.org/10.1029/2010JA015351>
- Matsumoto, Y., & Hoshino, M. (2004). Onset of turbulence induced by a Kelvin-Helmholtz vortex. *Geophysical Research Letters*, 31, L02807. <https://doi.org/10.1029/2003GL018195>
- Miura, A. (1999). Self-organization in the two-dimensional magnetohydrodynamic transverse Kelvin-Helmholtz instability. *Journal of Geophysical Research*, 104(A1), 395. <https://doi.org/10.1029/98JA02530>
- Moore, T. W., Nykyri, K., & Dimmock, A. P. (2016). Cross-scale energy transport in space plasmas. *Nature Physics*, 12, 1164–1169. <https://doi.org/10.1038/nphys3869>
- Nakamura, T. K. M., & Fujimoto, M. (2008). Magnetic effects on the coalescence of Kelvin-Helmholtz vortices. *Physical Review Letters*, 101(16), 1–4. <https://doi.org/10.1103/PhysRevLett.101.165002>
- Nakamura, T. K. M., Hayashi, D., Fujimoto, M., & Shinohara, I. (2004). Decay of MHD-scale Kelvin-Helmholtz vortices mediated by parasitic electron dynamics. *Physical Review Letters*, 92(14), 145001. <https://doi.org/10.1103/PhysRevLett.92.145001>
- Nykyri, K., & Otto, A. (2001). Plasma transport at the magnetospheric boundary due to reconnection in Kelvin-Helmholtz vortices. *Geophysical Research Letters*, 28, 3565–3568. <https://doi.org/10.1029/2001GL013239>
- Retinó, A. (2016). Space plasmas: A journey through scales. *Nature Physics*, 12, 1092–1093. <https://doi.org/10.1038/nphys3976>
- Robert, P., Roux, A., Harvey, C. C., Dunlop, M. W., Daly, P. W., & Glassmeier, K.-H. (1998). Tetrahedron geometric factors. *ISSI Scientific Report Series*, 001, 323–328.
- Roelof, E. C., & Sibeck, D. G. (1993). Magnetopause shape as a bivariate function of interplanetary magnetic field  $B_z$  and solar wind dynamic pressure. *Journal of Geophysical Research*, 98, 21,421–21,450. <https://doi.org/10.1029/93JA02362>
- Rossi, C., Califano, F., Retinó, A., Sorriso-Valvo, L., Henri, P., Servidio, S., et al. (2015). Two-fluid numerical simulations of turbulence inside Kelvin-Helmholtz vortices: Intermittency and reconnecting current sheets. *Physics of Plasmas*, 22(12), 122303. <https://doi.org/10.1063/1.4936795>
- Ryu, D., Jones, T. W., & Frank, A. (2000). The magnetohydrodynamic Kelvin-Helmholtz instability: A three-dimensional study of nonlinear evolution. *The Astrophysical Journal*, 545(1996), 475–493. <https://doi.org/10.1086/317789>
- Shen, C., Li, X., Dunlop, M., Liu, Z. X., Balogh, A., Baker, D. N., et al. (2003). Analyses on the geometrical structure of magnetic field in the current sheet based on Cluster measurements. *Journal of Geophysical Research*, 108(A5), 1168. <https://doi.org/10.1029/2002JA009612>
- Shen, C., Rong, Z. J., Dunlop, M. W., Ma, Y. H., Li, X., Zeng, G., et al. (2012). Spatial gradients from irregular, multiple-point spacecraft configurations. *Journal of Geophysical Research*, 117, A11207. <https://doi.org/10.1029/2012JA018075>
- Slavin, J. A., Acuña, M. H., Anderson, B. J., Baker, D. N., Benna, M., Gloeckler, G., et al. (2008). Mercury's magnetosphere after MESSENGER's first flyby. *Science*, 321, 85. <https://doi.org/10.1126/science.1159040>
- Takagi, K., Hashimoto, C., Hasegawa, H., Fujimoto, M., & TanDokoro, R. (2006). Kelvin-Helmholtz instability in a magnetotail flank-like geometry: Three-dimensional MHD simulations. *Journal of Geophysical Research*, 111, A08202. <https://doi.org/10.1029/2006JA011631>